

Finite-momentum pairing and superlattice superconductivity in valley-imbalanced rhombohedral graphene

Maine Christos,¹ Pietro M. Bonetti,¹ and Mathias S. Scheurer²

¹*Department of Physics, Harvard University, Cambridge MA 02138, USA*

²*Institute for Theoretical Physics III, University of Stuttgart, 70550 Stuttgart, Germany*

Inspired by the recent experimental discovery of superconductivity emerging from a time-reversal symmetry-breaking normal state in tetralayer rhombohedral graphene, we here investigate superconducting instabilities in this system. We classify the possible pairing instabilities, including states with commensurate and incommensurate center of mass momenta. As rotational symmetry is broken in the latter type of pairing states, their momentum-space structure is most naturally characterized by a “valley-independent Chern number”, measuring the relative chirality between the normal and superconducting state. We further demonstrate that superconductivity can condense at multiple incommensurate momenta simultaneously, leading to the spontaneous formation of a translational-symmetry-breaking superlattice superconductor. Studying multiple different pairing mechanisms and varying the degree of spin and valley polarization in the normal state, we compare the energetics of these superconductors. Our results demonstrate that valley-imbalanced rhombohedral tetralayer graphene can give rise to rich superconducting phenomenologies.

Not long after the discovery of superconductivity, correlated insulating, and symmetry-broken metallic phases in graphene-based moiré superlattices [1–3], it was shown that also non-twisted rhombohedral stacks of graphene layers can give rise to similar correlated physics [4–17]. Recently, the discovery of superconductivity emerging from a valley-imbalanced normal state in rhombohedral-stacked tetralayer graphene [18] has sparked a surge of interest [19–30].

Superconductivity in the presence of valley imbalance is remarkable since time-reversal symmetry (TRS) is broken—a key symmetry for superconductors, as it guarantees the degeneracy of Kramers partners forming Cooper pairs. As such, Cooper pairs are no longer expected to always have vanishing center of mass (COM) momentum [31] and the superconductor is predicted to become non-reciprocal, i.e., display a superconducting diode effect [32]. Furthermore, as the normal state is already chiral itself, the superconductor is by construction chiral too. Nonetheless, it is still a meaningful and important question to clarify how this chirality affects the orbital character of the superconducting state and how superconducting instabilities can be classified in light of the reduced symmetries. In analogy to topological superconductivity induced by coupling s -wave superconductors to chiral systems [33], one might wonder whether the normal state’s Berry curvature will always be inherited by the superconductor, making it topologically non-trivial, or whether it depends on microscopic energetic details.

In this work, we address these questions by a combination of symmetry-based classification of pairing and energetics. Using the continuum model [34, 35] of rhombohedral tetralayer graphene and multiple different interactions mediated by fluctuations of bosonic modes, including phonons and spin fluctuations, we find that sufficiently large valley polarization not only leads to in-

travalley pairing (commensurate center-of-mass momentum $2\mathbf{K}$), as expected, but also to pairing at finite momentum \mathbf{q} within the active valley (incommensurate net Cooper-pair momenta $2\mathbf{K} + \mathbf{q}$). While, at finite \mathbf{q} , one cannot use rotational symmetry to classify the orbital structure of the order parameter, we introduce a “valley-independent Chern number” \bar{C} , where $|\bar{C}| \neq 0$ corresponds to a topologically non-trivial superconducting state and the sign of \bar{C} encodes the relative chirality between the normal and superconducting phase. We find that, depending on the pairing mechanism and the normal state’s spin splitting, both topologically trivial and non-trivial phases are possible; for the latter, the chirality of the superconductor is found to be of the same orientation as that of the normal state ($\bar{C} > 0$) for all interactions we consider. Another important aspect is whether the order parameter condenses at a single wave vector \mathbf{q} (which we call a $1\text{-}\mathbf{q}$ state) or three C_{3z} -related wave vectors ($3\text{-}\mathbf{q}$ state). We find that microscopic parameters of the theory determine which scenario is energetically favored. While the $1\text{-}\mathbf{q}$ state preserves translational symmetry in observable quantities, the $3\text{-}\mathbf{q}$ state breaks it, leading to a superconducting superlattice. This can be detected in STM experiments [30] and is mathematically described in analogy to the continuum model of moiré graphene [36, 37], with interlayer terms corresponding to particle-hole couplings.

Model—We model the normal state for superconductivity with the single-particle Hamiltonian:

$$\mathcal{H}_c = \sum_{\mathbf{k}} \sum_{\eta, \sigma} c_{\mathbf{k}, \eta, \sigma}^\dagger (\epsilon_{\mathbf{k}, \eta} - \mu + \eta \mu_v + \sigma \mu_s) c_{\mathbf{k}, \eta, \sigma} \quad (1)$$

In the above, $\epsilon_{\mathbf{k}, \eta}$ is the dispersion of the active band of the continuum model of tetralayer rhombohedral graphene [11, 34, 35] at small, positive electron density

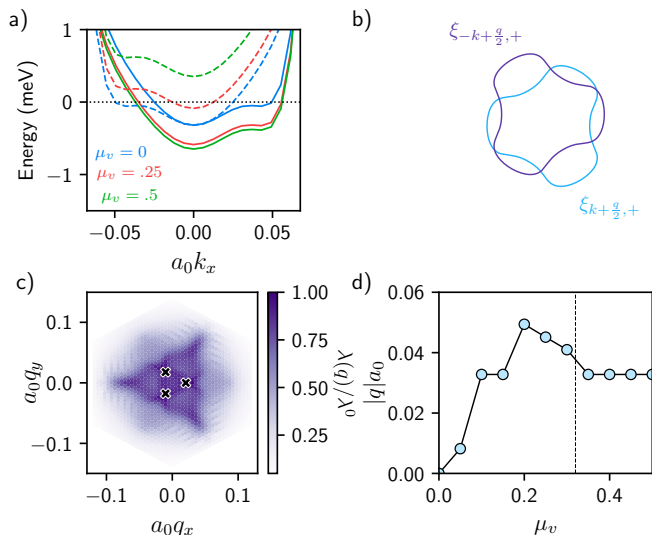


FIG. 1: Band structure (a) for different μ_v in + valley (solid lines) and - valley (dashed lines). In b), we illustrate the energetically favorable value of \mathbf{q} for a valley-polarized Fermi surface, leading to the maximum approximate overlap of the Fermi surfaces of $\xi_{\mathbf{k}+\frac{\mathbf{q}}{2},\eta,\sigma}$ and $\xi_{-\mathbf{k}+\frac{\mathbf{q}}{2},\eta,\sigma}$. (c) Normalized eigenvalue of the leading instability $\lambda(\mathbf{q})/\lambda^0$ for ferromagnetic fluctuations as a function of center-of-mass momentum \mathbf{q} for a fully valley-polarized and spin-degenerate normal state with global maxima marked by \times . In d), we plot the value of the Cooper pair center of mass momentum \mathbf{q} as a function of the amount of valley polarization μ_v for $\mu_s = 0$. The dashed black line denotes where the normal state becomes fully valley polarized.

and η and σ are summed over valley and spin indices, respectively. In all our numerics, we compute $\epsilon_{\mathbf{k},\eta}$ with the same model parameters given in [11]. We model spin and valley polarization in the normal state with μ_s and μ_v , which phenomenologically capture at a mean-field level the iso-spin symmetry breaking induced by electronic interactions at energy scales larger than those of the superconductor. The chemical potential μ is always adjusted such that the electron density is fixed to $n_e = 0.6 \times 10^{12} \text{ cm}^{-2}$, such that the density is near the value where valley-imbalanced superconductivity was observed in [18]. The band structure of Eq. (1) is plotted in Fig. 1a for different values of μ_v .

The model we consider has an $\text{SU}(2)_s$ spin rotation symmetry when $\mu_s = 0$, (spinless) TRS relating the two valleys when $\mu_v = 0$, and $\text{U}(1)$ valley symmetry for arbitrary $\mu_{s,v}$. Additionally, Eq. (1) is invariant under C_{3v} point group symmetries, generated by in-plane reflection σ_v and threefold rotation C_{3z} about the z axis. As will become important for our discussion of intravalley pairing below, we will choose the C_{3z} rotation axis to go through the A_1 sublattice and further take the phase of its representation in the microscopic 8-band model such that its A_1 - A_1 matrix element is 1 (see App. A).

We study interactions which originate from coupling the low-energy electrons to collective bosonic modes $\phi_j(\mathbf{q}) = \phi_j^\dagger(-\mathbf{q})$ with coupling of the form:

$$\mathcal{H}_{\text{fb}} = \sum_{\mathbf{k},\mathbf{p}} \sum_{\eta,\eta',\sigma,\sigma'} \phi_j(\mathbf{p}) c_{\mathbf{k},\eta,\sigma}^\dagger F_{\mathbf{k},\mathbf{p},j}^{\eta\sigma,\eta'\sigma'} c_{\mathbf{k}+\mathbf{p},\eta',\sigma'} \quad (2)$$

We impose the aforementioned symmetries also on the entire interacting Hamiltonian such that the transformation properties of the bosons ϕ_j under these symmetries are fully determined by the form factors (no summation convention) $F_{\mathbf{k},\mathbf{q},j}^{\eta\sigma,\eta'\sigma'} = \rho_j^{\eta\sigma,\eta'\sigma'} \langle u_{\eta\sigma}(\mathbf{k}) | u_{\eta'\sigma'}(\mathbf{k} + \mathbf{q}) \rangle$ where $|u_{\eta\sigma}(\mathbf{k})\rangle$ are the Bloch wavefunctions of the active band of the continuum model [34] and ρ is a 4×4 matrix in spin and valley space. For simplicity, we assume the coupling matrices ρ_j before band projection are momentum independent. For instance, ferromagnetic order-parameter fluctuations correspond to $\rho_j = (\sigma_x, \sigma_y, \sigma_z)\eta_0$. To also describe the attractive interactions coming from a phonon mode which transforms trivially under all symmetries, we will consider $\rho_j = \sigma_0\eta_0$.

Candidate pairing states—Before proceeding with energetics, let us classify the possible pairing instabilities based on symmetries. In its most general form, the superconducting order parameter $\Delta_{\mathbf{k},\mathbf{q}}$ is a matrix in spin and valley space and couples as

$$\mathcal{H}_{\text{MF}} = \sum_{\mathbf{k},\mathbf{q}} c_{\mathbf{k}+\frac{\mathbf{q}}{2},\eta,\sigma}^\dagger (\Delta_{\mathbf{k},\mathbf{q}})_{\eta\sigma,\eta'\sigma'} c_{-\mathbf{k}+\frac{\mathbf{q}}{2},\eta',\sigma'} + \text{H.c.} \quad (3)$$

to the electrons of the active band in Eq. (1). Fermionic anti-symmetry requires $\Delta_{\mathbf{k},\mathbf{q}} = -(\Delta_{-\mathbf{k},\mathbf{q}})^T$ and the presence of $\text{U}(1)_v$ symmetry implies that pairing is either entirely inter- or intravalley.

First focusing on $\mathbf{q} = 0$ in Eq. (3), the associated Cooper pairs have vanishing or lattice-commensurate COM momentum $2\mathbf{K}$ for inter- or intravalley pairing, respectively. In both cases, C_{3z} is preserved and we can use its irreducible representations (IRs) A , E , and E^* to classify pairing. While the latter two are degenerate in the presence of time-reversal symmetry, this is not the case for $\mu_v \neq 0$. If E is favored in one valley (one sign of μ_v), time-reversal implies that E^* is favored in the other (opposite sign of μ_v). To make a meaningful statement, we compute the Chern number C of the superconducting state, which can be expressed as a low-energy quantity in the single “active” valley using that time-reversal symmetry is preserved before the spontaneous emergence of valley polarization in the normal state. We also compute the net Berry flux Φ_N in the active valley within the continuum model, to provide a measure for its chirality. We then define the “valley-independent Chern number” as $\bar{C} := \text{sign}(\Phi_N)C$, which, as opposed to C itself, is independent of the sign of μ_v . A positive (negative) \bar{C} corresponds to a ferromagnetic (anti-ferromagnetic) coupling where the superconductor’s chirality is the same as

(opposite to) that of the normal state it emerges from. We checked by acting with the microscopic representation of C_{3z} on the superconducting states in our numerics that the A state is achiral, $\bar{C} = C = 0$, while E (E^*) has $\bar{C} = 1$ ($\bar{C} = -1$). We refer to Ref. 30 where the same conclusion is reached in a minimal two-band model.

As we will see below, also $\mathbf{q} \neq 0$ can be favored, corresponding to an incommensurate Cooper pair momentum. We will first start with a $1\text{-}\mathbf{q}$ state, i.e., $\Delta_{\mathbf{k},\mathbf{q}} = \delta_{\mathbf{q},\mathbf{q}_0} \Delta_{\mathbf{k}}^{\mathbf{q}_0}$ with $\mathbf{q}_0 \neq 0$. Importantly, at fixed $\mathbf{q}_0 \neq 0$, we cannot use C_{3z} and its IRs to classify pairing but we can still use \bar{C} . We emphasize that all of the superconductors discussed so far preserve translational symmetry in gauge-invariant observables. Below we will consider additional pairing states where this is not the case. Finally note that, for $\mu_s = 0$, all states further decay into spin-singlet and spin-triplet.

Leading $1\text{-}\mathbf{q}$ Instabilities—For a given choice of fluctuations as specified by ρ_j , we study the superconducting instabilities by solving the linearized mean-field gap equation of the normal-state Hamiltonian (2) supplemented with the electron-electron interaction generated by integrating out the bosons in Eq. (2). We choose a Lorentzian static susceptibility $\chi(\mathbf{q})$ for the bosons of the form $\chi(\mathbf{q}) = g^2 \frac{\alpha}{\alpha^2 + |\mathbf{q}|^2}$, where α can be thought of as a parameter quantifying how close the system is to criticality and g^2 represents the overall strength of the interaction relative to the kinetic energy.

Once $\mu_v \neq 0$ and time-reversal symmetry is broken, the states at \mathbf{k} and $-\mathbf{k}$ are no longer degenerate and consequently it is no longer necessarily energetically favorable to pair electrons at opposite momenta, and non-zero \mathbf{q} can become favorable. We note the precise value of \mathbf{q} strongly depends on details of the Fermi surface; however, as illustrated in Fig. 1b, \mathbf{q} is often approximately associated with the wave-vector for which there is the greatest approximate overlap between the shifted Fermi surfaces defined as $\epsilon_{\frac{\mathbf{q}}{2} \pm \mathbf{k}, \eta, \sigma} = 0$. To compute the value of \mathbf{q} and the associated order parameter $\Delta_{\mathbf{k}}^{\mathbf{q}}$, we solve the linearized gap equation for different values of \mathbf{q} and determine the leading instability from the value of \mathbf{q} with the largest leading eigenvalue λ , see Fig. 1c. A finite critical value of μ_v is necessary to obtain $\mathbf{q} \neq 0$, as a result of C_{3z} symmetry [32], although as shown in Fig. 1d, this critical value is small and beyond our numerical resolution for the underlying normal state we study.

While this behavior of \mathbf{q} is qualitatively the same for all pairing mechanisms we considered, the \mathbf{k} dependence of $\Delta_{\mathbf{k}}^{\mathbf{q}}$ is sensitive to the type of bosons mediating the interaction. Starting with ferromagnetic fluctuations, $\rho_j = (\sigma_x, \sigma_y, \sigma_z)\eta_0$, our results for varying degree of valley splitting μ_v are summarized in Fig. 2a-c. As expected for spin fluctuations, we find triplet pairing to be dominant. In the intervalley pairing regime at weak μ_v , the

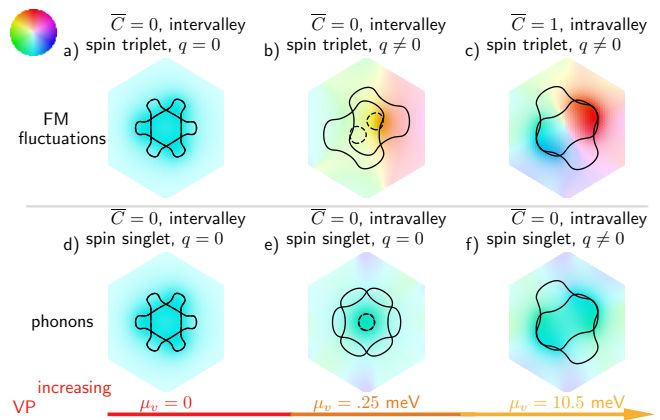


FIG. 2: We show the highest eigenvalue solutions of the linearized gap equation for spin ferromagnetic fluctuations (a-c) and phonons (d-f) for varying degree of valley polarization μ_v , with $\mu_s = 0$. For each solution, we show a single, nonzero magnitude component of $\Delta_{\mathbf{k}}^{\mathbf{q}}$ in the projected space of the active band, where the intensity and color indicate the magnitude and phase of $\Delta_{\mathbf{k}}^{\mathbf{q}}$ respectively. We also indicate \bar{C} and the state's spin structure. We take a displacement field $D = 110$ meV. For a discussion of how the gauge of the Bloch wavefunctions is fixed, see App. A.

anti-symmetry $\Delta_{\mathbf{k}}^{\mathbf{q}} = -(\Delta_{-\mathbf{k}}^{\mathbf{q}})^T$ does not constrain $\Delta_{\mathbf{k}}^{\mathbf{q}}$ to be even or odd in \mathbf{k} (see Fig. 2b) due to the valley degree of freedom. This changes for larger μ_v , where intravalley pairing is energetically favored and, hence, the triplet order parameter must be odd in \mathbf{k} , as one can see in Fig. 2c. The state in Fig. 2a clearly transforms under IR A but, as noted above, we cannot use the IRs of C_{3z} to classify the pairing states at finite \mathbf{q} as becomes apparent, e.g., in Fig. 2b. Instead, we use the signed Chern number \bar{C} of the superconductor and find that the initial $\bar{C} = 0$ state transitions to a superconductor with $\bar{C} = 1$, representing a ferromagnetic coupling between the normal state's and superconducting chirality.

The behavior is different for phonons, $\rho_j = \sigma_0 \eta_0$. In this case, the leading instability also condenses at finite \mathbf{q} above a critical value of μ_v , but remains topologically trivial ($\bar{C} = 0$) as valley polarization increases in Fig. 2d-f, with vanishing Chern number, $\bar{C} = 0$ (see App. E for definition of \bar{C} for the case with Fermi surfaces in both valleys).

3- \mathbf{q} states—So far, we just assumed that only one \mathbf{q} in Eq. (3) contributes. However, as can be seen in Fig. 1, C_{3z} symmetry requires that at least three \mathbf{q} be degenerate in the $\mathbf{q} \neq 0$ regime. In our numerical calculations, we find exactly three degenerate maxima in most cases (see Fig. 8). To take this into account, we write $\Delta_{\mathbf{k},\mathbf{q}} = \sum_{n=1}^3 \phi_n \delta_{\mathbf{q},\mathbf{q}_n} \Delta_{\mathbf{k}}^{\mathbf{q}_n}$, $\Delta_{\mathbf{k}}^{\mathbf{q}_n}$ being the eigenvector of the linearized gap equation, $\mathbf{q}_n = C_{3z}^{n-1} \mathbf{q}_1$, and expand

the free-energy as [38]

$$\mathcal{F} \sim r \sum_{n=1}^3 |\phi_n|^2 + u \left(\sum_{n=1}^3 |\phi_n|^2 \right)^2 + v \sum_{n,m>n} |\phi_n|^2 |\phi_m|^2 \quad (4)$$

where $u > \min\{0, -v\}$ as required by stability and we assumed a lattice-incommensurate value of \mathbf{q}_n . In the superconducting state, we have $r < 0$ and the sign of v determines whether we will have a $1\text{-}\mathbf{q}$ ($v > 0$) with only one of $\phi_{1,2,3}$ non-zero and the properties discussed above, or a $3\text{-}\mathbf{q}$ ($v < 0$) state, characterized by $|\phi_1| = |\phi_2| = |\phi_3|$. Note that the relative phase of ϕ_n just determines the origin of the emergent superconducting superlattice which preserves C_{3z} . The phases of theory (4) can be characterized by three gauge invariant *composite* order parameters $\varrho_{mn} = \phi_m \phi_n^*$ ($m \neq n$), describing charge density modulations with wave vector $\mathbf{q}_m - \mathbf{q}_n$ [39, 40]. It is obvious to see that the single- \mathbf{q} phase has all $\varrho_{mn} = 0$, while the $3\text{-}\mathbf{q}$ state has all three ϱ_{mn} nonzero and equal in absolute values.

To understand how microscopic parameters influence the nature of the finite- \mathbf{q} superconducting state, we consider a continuum model of spinless electrons with a $\mathbf{k}^2/(2m)$ dispersion coupled to a $p + ip$ -wave superconducting order parameter which carries a finite COM momentum. Additionally, we deform the electron dispersion with a *trigonal warping* term, whose strength we parametrize by w . Integrating out the electrons and expanding to quartic order in ϕ_n , we get expressions for the coefficients of Eq. (4) (App. D). In Fig. 3(a) we show that $u - \min\{0, -v\}$ is positive for all values of trigonal warping w and momentum $|\mathbf{q}|$ considered. In Fig. 3(b), we show v as a function of w and $|\mathbf{q}|$. We observe that at fixed w , a finite COM momentum is required to stabilize the $3\text{-}\mathbf{q}$ state.

Spectra—Finally, we will discuss the superconducting spectra in more detail. Starting with $\mathbf{q} = 0$, any infinitesimal order parameter with $|\Delta_{\mathbf{k}}^{\mathbf{q}=0}| \neq 0$ will immediately gap out the spectrum when $\mu_v = 0$. However, when $\mu_v \neq 0$ —similar to the case of inter-band pairing in twisted bilayer graphene [41, 42], where the states forming Cooper pairs are not degenerate either since they are in different bands—a finite amount of pairing strength is required for a full gap; below that, the system will generically have Bogoliubov Fermi surfaces [43]. At the same time, the thermal phase transition can become first order [41, 42] and whether there is a nodal regime close to T_c or not depends on microscopic details. We next turn to the scenario where $\mathbf{q} \neq 0$. In the case of the $1\text{-}\mathbf{q}$ state, as illustrated in Fig. 3c, the gap, which emerges at finite pairing strength $|\Delta|$, decreases and ultimately vanishes with increasing $|\mathbf{q}|$, as the splitting between the paired energies increases.

To compute the spectrum of the $3\text{-}\mathbf{q}$ state, we have to

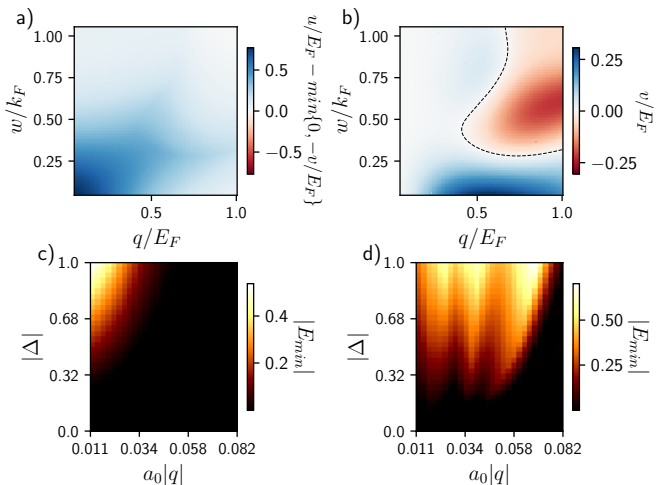


FIG. 3: In a) and b), we plot $u/E_F - \min\{0, -v/E_F\}$ and v/E_F , relevant to the Landau free energy in Eq. (4), as a function of center of mass momentum \mathbf{q} and w . We also compare the minimum excitation energy for the single- \mathbf{q} (c) and three- \mathbf{q} (d) for an intravalley spin-singlet gap function of the form $\Delta_{\mathbf{k}} = |\Delta|$.

take into account the broken translational symmetry and the associated superlattice reconstruction. This is done in analogy to the continuum model of twisted multilayer graphene [36, 37], where the superlattice now comes from the pairing terms. In practice, we use a continuum model with 17 shells of \mathbf{Q} vectors, which we find is sufficient to achieve convergence for our smallest $|\mathbf{q}|$ value. The resulting gap shown in Fig. 3b reveals that, similar to the case of the $1\text{-}\mathbf{q}$ state, a finite amount of pairing strength is needed at small \mathbf{q} to generate a gap, with the threshold pairing strength increasing as \mathbf{q} increases.

Other normal states—As at least one of the superconducting states in Ref. 18 is likely also spin polarized, we additionally comment on the effect of finite μ_s in Eq. (1). In our numerics, we found no qualitative changes in the features of the pairing states for $\mu_s \neq 0$ discussed so far, apart from sufficiently large μ_s leading to triplet pairing also for phonons. The main quantitative modification is that additional spin polarization lowers the critical μ_v for the formation of a topologically nontrivial superconductor ($\bar{C} = 1$), see App. B for details. We also have studied the case of ferromagnetic fluctuations with a higher displacement field such that the fully spin and valley polarized normal state has an annular Fermi surface. In this case we find the dominant instability always has $C = 0$, in agreement with the results of [21, 22, 26, 44]. We also study fluctuations of a valley polarized order (see App. C) with $\rho = \sigma_0 \eta_z$ for varying μ_s and μ_v . In this case we find the A state dominates when $\mu_s = 0$ with a finite μ_s leading to a transition to the E state.

Conclusion—We analyzed superconducting instabilities within a continuum model description of rhombohedral tetra-layer graphene as a function of spin and valley polarization. The analysis reveals rich superconducting physics, including the possibility of topological superconductivity and the spontaneous emergence of a superconducting superlattice. As discussed in [30], future scanning tunneling spectroscopy experiments will allow to probe key features of the identified candidate pairing states. We also note that a valley-imbalanced normal state will generically give rise to non-reciprocal superconductivity [32], with asymmetric current-voltage characteristics, providing a complementary way of accessing the reduced symmetries of the system.

Note added—Recently, a preprint [44] appeared that also discusses the relative chirality between the normal and superconducting state. The results agree where there is overlap (phonon-mediated pairing).

ACKNOWLEDGMENTS

The authors thank Subir Sachdev for comments on the manuscript. M.S.S. further thanks Denis Sedov for a collaboration on a related project [30]. M.C. and P.M.B. acknowledge funding from NSF grant DMR-2245246. P.M.B. acknowledges support by the German National Academy of Sciences Leopoldina through Grant No. LPDS 2023-06. M.S.S. further acknowledges funding by the European Union (ERC-2021-STG, Project 101040651—SuperCorr). Views and opinions expressed are however those of the authors only and do not necessarily reflect those of the European Union or the European Research Council Executive Agency. Neither the European Union nor the granting authority can be held responsible for them. M.S.S. is also grateful for support by grant NSF PHY-2309135 for his stay at the Kavli Institute for Theoretical Physics (KITP) where a part of the research was done.

-
- [1] E. Y. Andrei and A. H. MacDonald, “Graphene bilayers with a twist,” *Nature Materials* **19**, 1265 (2020).
- [2] L. Balents, C. R. Dean, D. K. Efetov, and A. F. Young, “Superconductivity and strong correlations in moiré flat bands,” *Nature Physics* **16**, 725 (2020).
- [3] K. P. Nuckolls and A. Yazdani, “A microscopic perspective on moiré materials,” *Nature Reviews Materials* **9**, 460 (2024).
- [4] H. Zhou, T. Xie, T. Taniguchi, K. Watanabe, and A. F. Young, “Superconductivity in rhombohedral trilayer graphene,” *Nature* **598**, 434 (2021).
- [5] H. Zhou, T. Xie, A. Ghazaryan, T. Holder, J. R. Ehrets, E. M. Spanton, T. Taniguchi, K. Watanabe, E. Berg, M. Serbyn, and A. F. Young, “Half- and quarter-metals in rhombohedral trilayer graphene,” *Nature* **598**, 429 (2021).
- [6] P. A. Pantaleón, A. Jimeno-Pozo, H. Sainz-Cruz, V. Phong, T. Cea, and F. Guinea, “Superconductivity and correlated phases in non-twisted bilayer and trilayer graphene,” *Nature Reviews Physics* **5**, 304 (2023).
- [7] Y.-Z. Chou, F. Wu, J. D. Sau, and S. Das Sarma, “Acoustic-phonon-mediated superconductivity in rhombohedral trilayer graphene,” *Phys. Rev. Lett.* **127**, 187001 (2021).
- [8] A. Ghazaryan, T. Holder, M. Serbyn, and E. Berg, “Unconventional superconductivity in systems with annular fermi surfaces: Application to rhombohedral trilayer graphene,” *Phys. Rev. Lett.* **127**, 247001 (2021).
- [9] Y.-Z. You and A. Vishwanath, “Kohn-luttinger superconductivity and intervalley coherence in rhombohedral trilayer graphene,” *Phys. Rev. B* **105**, 134524 (2022).
- [10] S. Chatterjee, T. Wang, E. Berg, and M. P. Zaletel, “Inter-valley coherent order and isospin fluctuation mediated superconductivity in rhombohedral trilayer graphene,” *Nature Communications* **13**, 6013 (2022).
- [11] A. Ghazaryan, T. Holder, E. Berg, and M. Serbyn, “Multilayer graphenes as a platform for interaction-driven physics and topological superconductivity,” *Phys. Rev. B* **107**, 104502 (2023).
- [12] A. Jimeno-Pozo, H. Sainz-Cruz, T. Cea, P. A. Pantaleón, and F. Guinea, “Superconductivity from electronic interactions and spin-orbit enhancement in bilayer and trilayer graphene,” *Phys. Rev. B* **107**, L161106 (2023).
- [13] A. L. Szabó and B. Roy, “Metals, fractional metals, and superconductivity in rhombohedral trilayer graphene,” *Phys. Rev. B* **105**, L081407 (2022).
- [14] W. Qin, C. Huang, T. Wolf, N. Wei, I. Blinov, and A. H. MacDonald, “Functional renormalization group study of superconductivity in rhombohedral trilayer graphene,” *Phys. Rev. Lett.* **130**, 146001 (2023).
- [15] Z. Li, X. Kuang, A. Jimeno-Pozo, H. Sainz-Cruz, Z. Zhan, S. Yuan, and F. Guinea, “Charge fluctuations, phonons, and superconductivity in multilayer graphene,” *Phys. Rev. B* **108**, 045404 (2023).
- [16] Z. Dong, L. Levitov, and A. V. Chubukov, “Superconductivity near spin and valley orders in graphene multilayers,” *Phys. Rev. B* **108**, 134503 (2023).
- [17] Z. Dong, É. Lantagne-Hurtubise, and J. Alicea, “Superconductivity from spin-canting fluctuations in rhombohedral graphene,” arXiv e-prints (2024), arXiv:2406.17036 [cond-mat.supr-con].
- [18] T. Han, Z. Lu, Y. Yao, L. Shi, J. Yang, J. Seo, S. Ye, Z. Wu, M. Zhou, H. Liu, G. Shi, Z. Hua, K. Watanabe, T. Taniguchi, P. Xiong, L. Fu, and L. Ju, “Signatures of chiral superconductivity in rhombohedral graphene,” (2024), arXiv:2408.15233.
- [19] Q. Qin and C. Wu, “Chiral finite-momentum superconductivity in the tetralayer graphene,” (2024), arXiv:2412.07145 [cond-mat.supr-con].
- [20] J. D. Sau and S. Wang, “Theory of anomalous hall effect from screened vortex charge in a phase disordered superconductor,” (2024), arXiv:2411.08969 [cond-mat.supr-con].

- con].
- [21] H. Yang and Y.-H. Zhang, “Topological incommensurate fulde-ferrell-larkin-ovchinnikov superconductor and bogoliubov fermi surface in rhombohedral tetra-layer graphene,” (2024), [arXiv:2411.02503 \[cond-mat.supr-con\]](#).
- [22] M. Geier, M. Davydova, and L. Fu, “Chiral and topological superconductivity in isospin polarized multilayer graphene,” (2024), [arXiv:2409.13829 \[cond-mat.supr-con\]](#).
- [23] Y.-Z. Chou, J. Zhu, and S. D. Sarma, “Intravalley spin-polarized superconductivity in rhombohedral tetralayer graphene,” (2024), [arXiv:2409.06701 \[cond-mat.supr-con\]](#).
- [24] G. Parra-Martinez, A. Jimeno-Pozo, V. Tien Phong, H. Sainz-Cruz, D. Kaplan, P. Emanuel, Y. Oreg, P. A. Pantaleon, J. A. Silva-Guillen, and F. Guinea, “Band Renormalization, Quarter Metals, and Chiral Superconductivity in Rhombohedral Tetralayer Graphene,” [arXiv e-prints \(2025\)](#), [2502.19474 \[cond-mat.str-el\]](#).
- [25] A. Jahin and S.-Z. Lin, “Enhanced Kohn-Luttinger topological superconductivity in bands with nontrivial geometry,” [arXiv e-prints \(2024\)](#), [arXiv:2411.09664 \[cond-mat.supr-con\]](#).
- [26] C. Yoon, T. Xu, Y. Barlas, and F. Zhang, “Quarter Metal Superconductivity,” [arXiv e-prints \(2025\)](#), [arXiv:2502.17555 \[cond-mat.mes-hall\]](#).
- [27] M. Kim, A. Timmel, L. Ju, and X.-G. Wen, “Topological chiral superconductivity beyond pairing in a fermi liquid,” [Physical Review B](#) **111** (2025), [10.1103/physrevb.111.014508](#).
- [28] P. H. Wilhelm, A. M. Läuchli, and M. S. Scheurer, “Ideal chern bands with strong short-range repulsion: Applications to correlated metals, superconductivity, and topological order,” [Phys. Rev. Res.](#) **6**, 043240 (2024).
- [29] B. A. Bernevig and Y. H. Kwan, ““Berry Trashcan” Model of Interacting Electrons in Rhombohedral Graphene,” [arXiv e-prints \(2025\)](#), [arXiv:2503.09692 \[cond-mat.str-el\]](#).
- [30] D. Sedov and M. S. Scheurer, “Probing superconductivity with tunneling spectroscopy in rhombohedral graphene,” [arXiv e-prints \(2024\)](#), [arXiv:2503.12650 \[cond-mat.supr-con\]](#).
- [31] Z. Han and S. A. Kivelson, “Pair density wave and reentrant superconducting tendencies originating from valley polarization,” [Phys. Rev. B](#) **105**, L100509 (2022).
- [32] H. D. Scammell, J. I. A. Li, and M. S. Scheurer, “Theory of zero-field superconducting diode effect in twisted trilayer graphene,” [2D Materials](#) **9**, 025027 (2022).
- [33] J. Alicea, “New directions in the pursuit of majorana fermions in solid state systems,” [Reports on Progress in Physics](#) **75**, 076501 (2012).
- [34] F. Zhang, B. Sahu, H. Min, and A. H. MacDonald, “Band structure of *abc*-stacked graphene trilayers,” [Phys. Rev. B](#) **82**, 035409 (2010).
- [35] M. Koshino and E. McCann, “Trigonal warping and berry’s phase $n\pi$ in *abc*-stacked multilayer graphene,” [Phys. Rev. B](#) **80**, 165409 (2009).
- [36] J. M. B. L. Dos Santos, N. M. R. Peres, and A. H. C. Neto, “Graphene bilayer with a twist: electronic structure,” [Phys. Rev. Lett.](#) **99**, 256802 (2007).
- [37] R. Bistritzer and A. H. MacDonald, “Moiré bands in twisted double-layer graphene,” [Proc. Natl. Acad. Sci. U.S.A.](#) **108**, 12233 (2011).
- [38] Note that in the spin unpolarized case, due to the system’s SU(2) invariance under spin rotations, one can write the order parameter as $\Delta_{\mathbf{k},\mathbf{q}}^{\eta\sigma,\eta'\sigma'}$ as $\sum_{n=1}^3 \vec{\phi}_n \cdot (i\sigma_y \vec{\sigma})_{\sigma\sigma'} \delta_{\eta\eta'} \Delta_{\mathbf{k}}^{q_n} \delta_{\mathbf{q},\mathbf{q}_n}$, thereby promoting $\vec{\phi}_n$ to a complex vector. In this case the Landau theory is invariant under O(3) rotations of $\vec{\phi}_n$ and it allows for more quartic terms than the ones in Eq. (4). Additionally, more phases than the two discussed here are in principle possible.
- [39] D. F. Agterberg, J. S. Davis, S. D. Edkins, E. Fradkin, D. J. Van Harlingen, S. A. Kivelson, P. A. Lee, L. Radzihovsky, J. M. Tranquada, and Y. Wang, “The physics of pair-density waves: Cuprate superconductors and beyond,” [Annual Review of Condensed Matter Physics](#) **11**, 231 (2020).
- [40] S. Zhou and Z. Wang, “Chern fermi pocket, topological pair density wave, and charge-4e and charge-6e superconductivity in kagomé superconductors,” [Nature Communications](#) **13** (2022), [10.1038/s41467-022-34832-2](#).
- [41] M. Christos, S. Sachdev, and M. S. Scheurer, “Nodal band-off-diagonal superconductivity in twisted graphene superlattices,” [Nature Communications](#) **14** (2023), [10.1038/s41467-023-42471-4](#).
- [42] B. Putzer and M. S. Scheurer, “Eliashberg theory and superfluid stiffness of band-off-diagonal pairing in twisted graphene,” (2025), [arXiv:2501.12435 \[cond-mat.supr-con\]](#).
- [43] P. M. R. Brydon, D. F. Agterberg, H. Menke, and C. Timm, “Bogoliubov fermi surfaces: General theory, magnetic order, and topology,” [Phys. Rev. B](#) **98**, 224509 (2018).
- [44] J. May-Mann, T. Helbig, and T. Devakul, “How pairing mechanism dictates topology in valley-polarized superconductors with Berry curvature,” [arXiv e-prints \(2025\)](#), [2503.05697 \[cond-mat.supr-con\]](#).
- [45] A. Ghazaryan, T. Holder, E. Berg, and M. Serbyn, “Multilayer graphenes as a platform for interaction-driven physics and topological superconductivity,” [Physical Review B](#) **107** (2023), [10.1103/physrevb.107.104502](#).

Appendix A: Model and Linearized Gap Equation

In this appendix, we describe the microscopic continuum model we take as our starting point and give the full gap equation we solve in the main text. We take the model of [34, 45] in a single valley:

$$\mathcal{H} = \sum_{\mathbf{k}} c_{\mathbf{k}}^{\dagger} \mathcal{H}_{\mathbf{k}} c_{\mathbf{k}} \quad \mathcal{H}_{\mathbf{k}} = \begin{pmatrix} \delta + D/2 & v_0\pi^{\dagger} & v_4\pi^{\dagger} & v_3\pi & 0 & \gamma_2/2 & 0 & 0 \\ v_0\pi & D/2 & \gamma_1 & v_4\pi^{\dagger} & 0 & 0 & 0 & 0 \\ v_4\pi & \gamma_1 & D/6 & v_0\pi^{\dagger} & v_4\pi^{\dagger} & v_3\pi & 0 & \gamma_2/2 \\ v_3\pi^{\dagger} & v_4\pi & v_0\pi & D/6 & \gamma_1 & v_4\pi^{\dagger} & 0 & 0 \\ 0 & 0 & v_4\pi & \gamma_1 & -D/6 & v_0\pi^{\dagger} & v_4\pi^{\dagger} & v_3\pi \\ \gamma_2/2 & 0 & v_3\pi^{\dagger} & v_4\pi & v_0\pi & -D/6 & \gamma_1 & v_4\pi^{\dagger} \\ 0 & 0 & 0 & 0 & v_4\pi & \gamma_1 & -D/2 & v_0\pi^{\dagger} \\ 0 & 0 & \gamma_2/2 & 0 & v_3\pi^{\dagger} & v_4\pi & v_0\pi & \delta - D/2 \end{pmatrix} \quad (\text{A1})$$

where $\pi = k_x + ik_y$ and $v_i = \frac{\sqrt{3}a_0}{2}\gamma_i$ where $a_0 = 0.246$ nm. We use the parameter values of [11], taking $\gamma_0 = 3.1$ eV, $\gamma_1 = 0.38$ eV, $\gamma_2 = -0.015$ eV, $\gamma_3 = 0.29$ eV, $\gamma_4 = -0.141$ eV, and $\delta = -0.0105$ eV. The Hamiltonian in the opposite valley is obtained by acting a spinless time-reversal symmetry \mathcal{T} on Eq. A1, which acts on the electrons in the microscopic basis as $\mathcal{T} : c_{\mathbf{k},l,\rho,\eta} \rightarrow c_{-\mathbf{k},l,\rho,-\eta}^{\dagger}$ (here ρ and $l = 1, 2, 3, 4$ label the sublattice and layer degrees of freedom respectively). There is also a threefold rotation symmetry we denote as C_{3z} (which is always present, including when $\mu_v \neq 0$) which acts as $C_{3z} : c_{\mathbf{k},\rho\eta} \rightarrow [e^{-i2\pi/3(\rho_z+l+1)}]_{\rho\eta;\rho'\eta'} c_{C_{3z}(\mathbf{k}),\rho'\eta'}$.

We then consider taking only the active band of Eq. A1 at small doping and add interactions generated by coupling the electrons to an arbitrary bosonic mode ϕ_j as in Eq. 2:

$$\mathcal{H}_{int} = \frac{1}{A} \sum_{\mathbf{p}} \chi_{\mathbf{p}} \rho_j(\mathbf{p}) \rho_j(-\mathbf{p}) \quad (\text{A2})$$

We decouple this interaction in the cooper channel allowing for nonzero expectation values of the bilinear (written in terms of the projected degrees of freedom $c_{\mathbf{k},\eta,\sigma}$ now labeled only by spin σ and valley η):

$$\langle c_{\mathbf{k},\eta\sigma} c_{\mathbf{k}',\eta'\sigma'} \rangle \sim \delta_{\mathbf{k}-\frac{\mathbf{q}}{2}, -\mathbf{k}'+\frac{\mathbf{q}}{2}} \quad (\text{A3})$$

In this channel, the mean-field Hamiltonian is:

$$\mathcal{H}_{MF} = \mathcal{H}_{kin} + \sum_{\mathbf{k}} c_{\mathbf{k}+\frac{\mathbf{q}}{2},\eta,\sigma}^{\dagger} (\Delta_{\mathbf{k}}^{\mathbf{q}})^{\eta\sigma,\eta'\sigma'} c_{-\mathbf{k}+\frac{\mathbf{q}}{2},\eta',\sigma'} + \text{h.c.} \quad (\text{A4})$$

where \mathcal{H}_{kin} is the dispersion of the active band of Eq. A1 and as in the main text we have defined:

$$(\Delta_{\mathbf{k}}^{\mathbf{q}})^{\eta\sigma,\eta'\sigma'} = \sum_{\mathbf{p}} \chi_{\mathbf{p}} \langle c_{-\mathbf{k}-\mathbf{p}+\frac{\mathbf{q}}{2},\tau\alpha} c_{\mathbf{k}+\mathbf{p}+\frac{\mathbf{q}}{2},\tau'\alpha'} \rangle F_{\mathbf{k}+\frac{\mathbf{q}}{2},\mathbf{p}}^{\eta\sigma,\tau'\alpha'} F_{-\mathbf{k}+\frac{\mathbf{q}}{2},-\mathbf{p}}^{\eta'\sigma',\tau\alpha} \quad (\text{A5})$$

In our numerics, we fix the gauge of the bloch wavefunctions used to compute $F_{\mathbf{k}+\frac{\mathbf{q}}{2},\mathbf{p}}^{\eta\sigma,\tau'\alpha'}$ by choosing a test wave function of the continuum model $|u(\mathbf{k}^0)\rangle$ at momentum $|\mathbf{k}^0| \gg k_F$ and fixing the phases of the bloch wavefunctions such that $\langle u(\mathbf{k}^0)|u_{\eta}(\mathbf{k})\rangle / |\langle u(\mathbf{k}^0)|u_{\eta\sigma}(\mathbf{k})\rangle| = 1$ for \mathbf{k} within the extent we study numerically and wavefunctions $|u_{\eta\sigma}(\mathbf{k})\rangle$ in the active band of the continuum model at small doping. For intervalley pairings, we further use time-reversal symmetry to fix $\langle u_{+,\sigma}(\mathbf{k}^0)|u_{-,\sigma}(-\mathbf{k})^*\rangle = 1$. We note that a variational mean-field solution for the gap $(\Delta_{\mathbf{k}}^{\mathbf{q}})^{\eta\sigma,\eta'\sigma'}$ generically depends on two momenta, \mathbf{k} and the COM momenta \mathbf{q} . Minimization of the free energy associated with Eq. A4 leads to the following self-consistency equation valid when $\Delta_{\mathbf{k}}^{\mathbf{q}} \rightarrow 0$:

$$(\Delta_{\mathbf{k}}^{\mathbf{q}})^{\eta\sigma,\eta'\sigma'} = -\frac{1}{A} \sum_{\mathbf{p}} \sum_{\tau,\tau'=\uparrow,\downarrow,\alpha,\beta=\pm} \chi_{\mathbf{p}} F_{\mathbf{k}+\frac{\mathbf{q}}{2},\mathbf{p}}^{\eta\sigma,\tau'\beta} F_{-\mathbf{k}+\frac{\mathbf{q}}{2},-\mathbf{p}}^{\eta'\sigma',\tau\alpha} \left(\frac{n_F(\xi_{\mathbf{k}+\mathbf{p}+\frac{\mathbf{q}}{2}}^{\tau'\beta}) - n_F(-\xi_{-\mathbf{k}-\mathbf{p}+\frac{\mathbf{q}}{2}}^{\tau\alpha})}{\xi_{\mathbf{k}+\mathbf{q}+\frac{\mathbf{q}}{2}}^{\tau'\beta} + \xi_{-\mathbf{k}-\mathbf{p}+\frac{\mathbf{q}}{2}}^{\tau\alpha}} \right) (\Delta_{\mathbf{k}+\mathbf{p}}^{\mathbf{q}})^{\tau\alpha,\tau'\beta} \quad (\text{A6})$$

In the above, $\xi_{\mathbf{k}}^{\eta\sigma} = \epsilon_{\mathbf{k},\eta,\sigma} + \eta\mu_v + \sigma\mu_s$. We solve this linear equation for our various choices of normal states on a grid with 1657 \mathbf{k} points and \mathbf{q} points for each normal state.

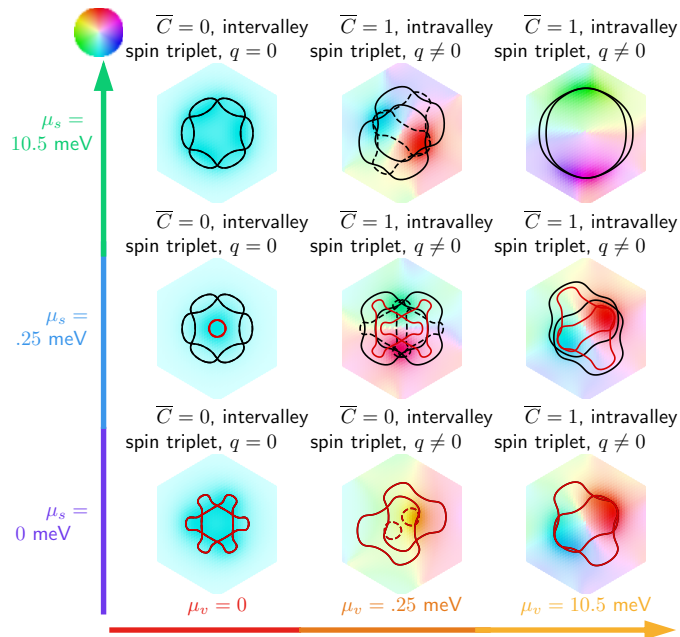


FIG. 4: We plot the leading solution $\Delta_{\mathbf{k}}^q$ for ferromagnetic fluctuations ($\rho^i = (s_x, s_y, s_z)\eta_0$) as a function of varying amounts of spin and valley polarization in the normal state of superconductivity. We also plot the normal state Fermi surfaces for the + (solid lines) and - (dashed lines) valleys and \uparrow (black) and \downarrow (red) Fermi surfaces. We also use “spin singlet” to refer to anti-symmetric pairing between spins and “spin triplet” to refer a symmetric pairing state with respect to spin when $\mu_s \neq 0$ and $SU(2)_s$ spin symmetry is broken. We solve the linearized gap equation with displacement field $D = 110$ meV. We observe a tendency towards a state with $\bar{C} = +1$ relative to the normal state with increasing valley polarization.

Appendix B: Different Normal States

In this appendix, we will study the impact of changing the underlying normal state on the leading superconducting instabilities. As shown in Fig. 8 and discussed in the main text, finite μ_v will generically result in finite \mathbf{q} pairing. We next consider the impact of spin polarization on the leading instabilities by varying the amount of spin and valley polarization by adjusting $\mu_{s,v}$ in Eq. 1. The results for ferromagnetic fluctuations are shown in Fig. 4. We find adding partial spin polarization ($\mu_s \neq 0$ such that both spin flavors both have active Fermi surfaces) pushes the leading instability to the E state for smaller valley polarization as modeled by μ_v .

We then study ferromagnetic fluctuation mediated superconductivity for a normal state with a higher displacement field, such that the fully spin and valley polarized normal state has an annular Fermi surface. The results are shown in Fig. 5. We find that the state always has $\bar{C} = 0$ in agreement with the results of [21, 22, 26, 44]. Finally, we study the linearized gap equation for phonons ($\rho^i = s_0\eta_0$) for varying amounts of spin and valley polarization. The results are shown in Fig. 6.

Appendix C: Fluctuations of Valley Polarized Order

In this appendix we discuss the leading superconducting instabilities for the case of valley polarized fluctuations (ie $\rho = \eta_z s_0$). Our results are shown in Fig. 7. We find an intravalley state is favored for all values of μ_v and μ_s , with a transition to a state with $\bar{C} = 1$ occurring for sufficient spin polarization. A finite- \mathbf{q} state is also favored in the spin polarized case even when $\mu_v = 0$, as a consequence of disfavored pairing between Kramers partners for this type of interaction.

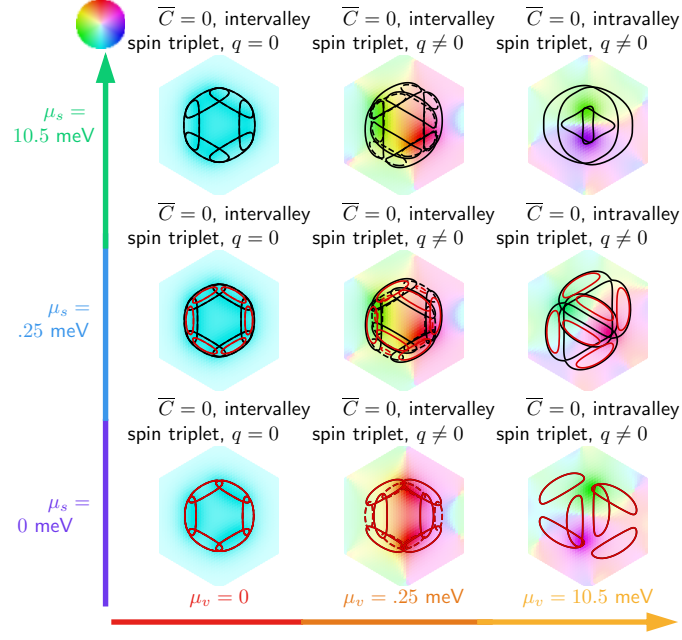


FIG. 5: We plot the leading solution $\Delta_{\mathbf{k}}^q$ for ferromagnetic fluctuations ($\rho^i = (s_x, s_y, s_z)\eta_0$) as a function of varying amounts of spin and valley polarization in the normal state of superconductivity, for a normal state at the same doping of $n_e = 0.6 \times 10^{12} \text{ cm}^{-2}$ but now at a higher displacement field $D = 140 \text{ meV}$. We plot the normal state Fermi surfaces for the + (solid lines) and - (dashed lines) valleys and \uparrow (black) and \downarrow (red) Fermi surfaces.

Appendix D: Microscopic evaluation of Landau coefficients

In this appendix, we derive and discuss the microscopic expressions for the coefficients of the Landau theory in Eq. (4). We start from a continuum model of spinless electrons with a trigonal warping term (parametrized by w) coupled to a $p + ip$ -wave superconducting order parameter:

$$\mathcal{H} = \sum_{\mathbf{k}} \xi_{\mathbf{k}} c_{\mathbf{k}}^\dagger c_{\mathbf{k}} + \sum_{\mathbf{k}, \mathbf{q}} [e^{i\theta_{\mathbf{k}}} c_{\mathbf{q}/2-\mathbf{k}} c_{\mathbf{q}/2+\mathbf{k}} \Delta_{\mathbf{q}}^* + \text{h.c.}] , \quad (\text{D1})$$

with $\xi_{\mathbf{k}} = \frac{k^2}{2m} [1 + w \cos(3\theta_{\mathbf{k}})] - \mu$, μ being the chemical potential and m the electron mass, and $e^{i\theta_{\mathbf{k}}} = \frac{k_x + ik_y}{|\mathbf{k}|}$. We write $\Delta_{\mathbf{q}} = \sum_{n=1}^3 \phi_n \delta_{\mathbf{q}, \mathbf{q}_n}$, where \mathbf{q}_n are three C_{3z} -related wave vectors given by $\mathbf{q}_1 = |q|(1, 0)$, $\mathbf{q}_2 = |q|(-1/2, \sqrt{3}/2)$, and $\mathbf{q}_3 = |q|(-1/2, -\sqrt{3}/2)$. Integrating out the electrons and expanding the effective action up to fourth order in ϕ_n , we obtain Eq. (4). The coefficients u and v are given by

$$u = I_1 \quad (\text{D2a})$$

$$v = 2I_2 - 2I_1 , \quad (\text{D2b})$$

where the integrals I_1 and I_2 read

$$I_1 = \int_{\mathbf{k}} \left[2 \frac{n_F(-\xi_{\mathbf{q}_1-\mathbf{k}}) - n_F(\xi_{\mathbf{k}})}{(\xi_{\mathbf{k}} + \xi_{\mathbf{q}_1-\mathbf{k}})^3} + \frac{n'_F(-\xi_{\mathbf{q}_1-\mathbf{k}}) + n'_F(\xi_{\mathbf{k}})}{(\xi_{\mathbf{k}} + \xi_{\mathbf{q}_1-\mathbf{k}})^2} \right] , \quad (\text{D3a})$$

$$I_2 = \int_{\mathbf{k}} \left[- \frac{(2\xi_{\mathbf{k}} + \xi_{\mathbf{q}_1-\mathbf{k}} + \xi_{\mathbf{q}_2-\mathbf{k}})}{(\xi_{\mathbf{k}} + \xi_{\mathbf{q}_1-\mathbf{k}})^2 (\xi_{\mathbf{k}} + \xi_{\mathbf{q}_2-\mathbf{k}})^2} n_F(\xi_{\mathbf{k}}) + \frac{n_F(-\xi_{\mathbf{q}_2-\mathbf{k}})}{(\xi_{\mathbf{k}} + \xi_{\mathbf{q}_2-\mathbf{k}})^2 (\xi_{\mathbf{q}_1-\mathbf{k}} - \xi_{\mathbf{q}_2-\mathbf{k}})} \right. \\ \left. - \frac{n_F(-\xi_{\mathbf{q}_1-\mathbf{k}})}{(\xi_{\mathbf{k}} + \xi_{\mathbf{q}_1-\mathbf{k}})^2 (\xi_{\mathbf{q}_1-\mathbf{k}} - \xi_{\mathbf{q}_2-\mathbf{k}})} + \frac{n'_F(\xi_{\mathbf{k}})}{(\xi_{\mathbf{k}} + \xi_{\mathbf{q}_1-\mathbf{k}})(\xi_{\mathbf{k}} + \xi_{\mathbf{q}_2-\mathbf{k}})} \right] , \quad (\text{D3b})$$

with $n_F(x) = 1/(e^{x/T} + 1)$ the Fermi distribution function at temperature T and $n'_F(x) = \frac{dn_F}{dx}$. In the above equations the momentum integrals have to be intended as $\int_{\mathbf{k}} = \int_0^\Lambda \frac{|\mathbf{k}|d|\mathbf{k}|}{2\pi} \int_0^{2\pi} \frac{d\theta_{\mathbf{k}}}{2\pi}$. In the numerical evaluation of the coefficients in Fig. 3 we have chosen $\Lambda = 10k_F$ with $k_F = \sqrt{2m\mu}$ and a temperature of $T = E_F/4$, with $E_F = \mu$.

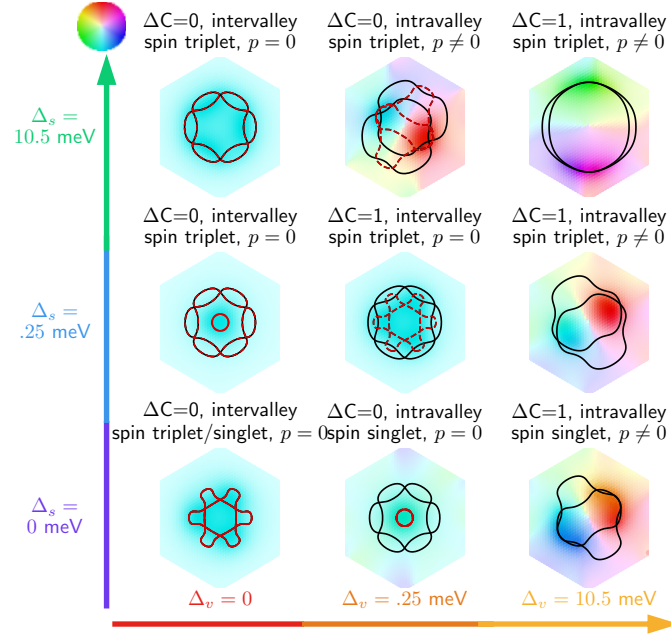


FIG. 6: We plot the leading solution $\Delta_{\mathbf{k}}^q$ for phonons ($\rho^i = s_0 \eta_0$) as a function of varying amounts of spin and valley polarization in the normal state of superconductivity.

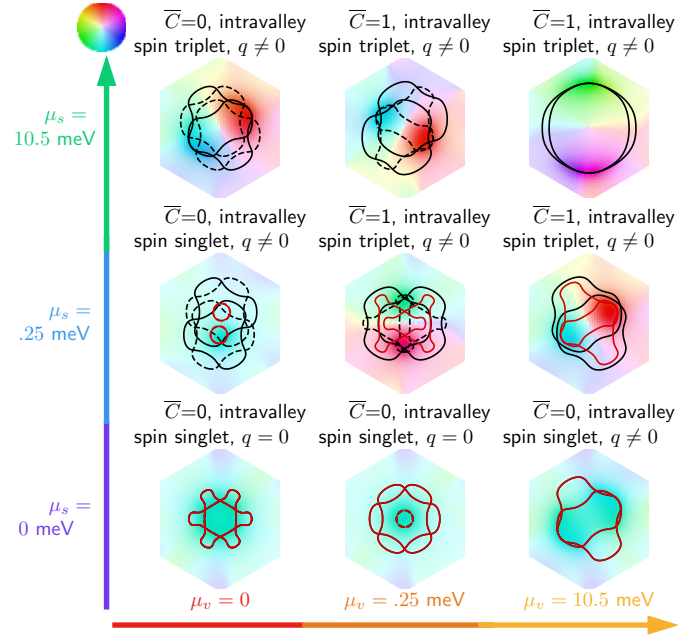


FIG. 7: We plot the leading solution $\Delta_{\mathbf{k}}^q$ for fluctuations of a valley polarized order ($\rho^i = s_0 \eta_z$) as a function of varying amounts of spin and valley polarization in the normal state of superconductivity.

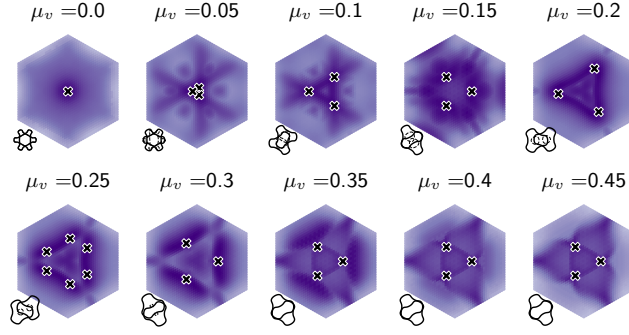


FIG. 8: We plot the leading eigenvalue $\lambda(\mathbf{q})$ corresponding to each $\Delta_{\mathbf{k}}^q$ as a function of center of mass momentum \mathbf{q} , for varying amounts of valley polarization and $\mu_s = 0$. Maxima are marked with a x marker.

Appendix E: Chern Number

In this appendix, we will describe how the Chern number of each superconducting state is computed within the continuum model description of App. A. For each pairing state, we construct the mean-field Hamiltonian:

$$H_{BdG} = \sum_{\mathbf{k}} \Psi_{\mathbf{k}}^{\dagger} \begin{pmatrix} \tilde{\epsilon}_{\mathbf{k},\mathbf{q}} & \Delta_{\mathbf{k}}^q \\ (\Delta_{\mathbf{k}}^q)^{\dagger} & -\tilde{\epsilon}_{-\mathbf{k},\mathbf{q}} \end{pmatrix} \Psi_{\mathbf{k}} \quad (\text{E1})$$

Where $\Psi_{\mathbf{k}}$ is a vector defined for each \mathbf{k} on half the Brillouin zone as:

$$\Psi_{\mathbf{k}} = \left(c_{\mathbf{k}+\frac{\mathbf{q}}{2},\uparrow,+}, c_{\mathbf{k}+\frac{\mathbf{q}}{2},\downarrow,+}, c_{\mathbf{k}+\frac{\mathbf{q}}{2},\uparrow,-}, c_{\mathbf{k}+\frac{\mathbf{q}}{2},\downarrow,-}, c_{-\mathbf{k}+\frac{\mathbf{q}}{2},\uparrow,+}^{\dagger}, c_{-\mathbf{k}+\frac{\mathbf{q}}{2},\downarrow,+}^{\dagger}, c_{-\mathbf{k}+\frac{\mathbf{q}}{2},\uparrow,-}^{\dagger}, c_{-\mathbf{k}+\frac{\mathbf{q}}{2},\downarrow,-}^{\dagger} \right)^T \quad (\text{E2})$$

and $\tilde{\epsilon}_{\mathbf{k},\mathbf{q}}$ is the diagonal matrix constructed from the dispersions of each spin and valley flavor:

$$\tilde{\epsilon}_{\mathbf{k},\mathbf{q}} = \text{Diag} \left(\xi_{\mathbf{k}+\frac{\mathbf{q}}{2},\uparrow,+}, \xi_{\mathbf{k}+\frac{\mathbf{q}}{2},\downarrow,+}, \xi_{\mathbf{k}+\frac{\mathbf{q}}{2},\uparrow,-}, \xi_{\mathbf{k}+\frac{\mathbf{q}}{2},\downarrow,-} \right) \quad (\text{E3})$$

and $\Delta_{\mathbf{k}}^q$ is the matrix defined in Eq. A5. For a given band of Eq. E1 with corresponding set of eigenvectors at each \mathbf{k} point labeled as $a_{\mathbf{k}}$, we compute the Chern number of the superconducting state as:

$$C = \frac{1}{2\pi} \int_{BZ} d^2\mathbf{k} \quad \Omega^{SC}(\mathbf{k}) \quad (\text{E4})$$

where $\Omega^{SC}(\mathbf{k})$ is the Berry curvature of the superconducting state, and is defined as:

$$\Omega_{\mathbf{k}}^{SC} = \text{Im} [\log (U_{\mathbf{k},\mathbf{k}+\delta\mathbf{k}\hat{x}} U_{\mathbf{k}+\delta\mathbf{k}\hat{x},\mathbf{k}+\delta\mathbf{k}\hat{x}+\delta\mathbf{k}\hat{y}} U_{\mathbf{k}+\delta\mathbf{k}\hat{x}+\delta\mathbf{k}\hat{y},\mathbf{k}+\delta\mathbf{k}\hat{y}} U_{\mathbf{k}+\delta\mathbf{k}\hat{y},\mathbf{k}})] \quad (\text{E5})$$

where $U_{\mathbf{k},\mathbf{k}'} = a_{\mathbf{k}}^{\dagger} \begin{pmatrix} F(\mathbf{k} + \frac{\mathbf{q}}{2}, \mathbf{k}' - \mathbf{k}) & 0 \\ 0 & F^*(-\mathbf{k} + \frac{\mathbf{q}}{2}, -\mathbf{k}' + \mathbf{k}) \end{pmatrix} a_{\mathbf{k}'}$

$$U_{\mathbf{k},\mathbf{k}'} = a_{\mathbf{k}}^{\dagger} \begin{pmatrix} F(\mathbf{k} + \frac{\mathbf{q}}{2}, \mathbf{k}' - \mathbf{k}) & 0 \\ 0 & F^*(-\mathbf{k} + \frac{\mathbf{q}}{2}, -\mathbf{k}' + \mathbf{k}) \end{pmatrix} a_{\mathbf{k}'} \quad \Omega(\mathbf{k}) = \text{Im} [\log (U_{\mathbf{k}_1,\mathbf{k}_2} U_{\mathbf{k}_2,\mathbf{k}_3} U_{\mathbf{k}_3,\mathbf{k}_4} U_{\mathbf{k}_4,\mathbf{k}_1})] \quad (\text{E6})$$

Our continuum model has a cutoff $|\mathbf{\Lambda}| > k_F$ within each valley (in our computations we use a hexagonal momentum space grid with a \mathbf{k} dependent cutoff, though this does not affect the following argument) and we may break the berry curvature into two contributions, one for integrand with $|\mathbf{k}| < |\mathbf{\Lambda}|$ and one for integrand with $|\mathbf{k}| > |\mathbf{\Lambda}|$, such that we may write:

$$C_{SC} = \frac{1}{2\pi} \int_{|\mathbf{k}| < |\mathbf{\Lambda}|} d^2\mathbf{k} \quad \Omega_{\mathbf{k}}^{SC} + \frac{1}{2\pi} \int_{|\mathbf{k}| > |\mathbf{\Lambda}|} d^2\mathbf{k} \quad \Omega_{\mathbf{k}}^{SC} \quad (\text{E7})$$

We note that for cases where the normal state is totally valley polarized, we are taking the cutoff $|\mathbf{\Lambda}|$ to be within only the single, active valley. For cases where the pairing is valley polarized but the normal state still has active Fermi

surfaces in both valleys, we compute the Chern number only for the valley in which the pairing is active (although our definition of C is still well-defined and quantized in this case, we note that quantized response would not be observed due to the presence of the active Fermi surface in the other valley). For cases with an intervalley pairing, we take a cutoff $|\Lambda|$ in both valleys and compute the Chern number.

If $|\Delta_{\mathbf{k}}^q|$ is sufficiently small for $|\mathbf{k}| > |\Lambda|$, the second contribution may be rewritten as:

$$\frac{1}{2\pi} \int_{|\mathbf{k}| > |\Lambda|} d^2\mathbf{k} \Omega_{\mathbf{k}}^{SC} = -\frac{1}{2\pi} \int_{|\mathbf{k}| > |\Lambda|} d^2\mathbf{k} \Omega_{\mathbf{k}}^{\phi} = \frac{1}{2\pi} \int_{|\mathbf{k}| < |\Lambda|} d^2\mathbf{k} \Omega_{\mathbf{k}}^{\phi} \quad (\text{E8})$$

where $\Omega_{\mathbf{k}}^{\phi}$ is the Berry curvature of the normal state Bloch wavefunction. In the above we have used that the Berry curvature integrated over the entire band (including both valleys of the continuum model) must be 0. In this case, we have an expression for the Berry curvature defined for integrands only within our momentum cutoff:

$$C_{SC} = \frac{1}{2\pi} \int_{|\mathbf{k}| < |\Lambda|} d^2\mathbf{k} \Omega_{\mathbf{k}}^{SC} + \frac{1}{2\pi} \int_{|\mathbf{k}| < |\Lambda|} d^2\mathbf{k} \Omega_{\mathbf{k}}^{\phi} \quad (\text{E9})$$

Appendix F: 3-q state gap

In this appendix, we discuss how the minimum excitation gap is computed for the 3- \mathbf{q} state for a finite \mathbf{q} , momentum independent pairing $\Delta_{\mathbf{k}}^p = |\Delta|$. For simplicity, we assume spin singlet pairing ($\mu_s = 0$) and only a single active valley with dispersion $\xi_{\mathbf{k}}$ (we will suppress valley indices in our discussion going forward). We then consider adding a term with the following form in real space:

$$\mathcal{H}_{pair} = \sum_{\mathbf{i}} \sum_j c_{\mathbf{i},\uparrow}^{\dagger} c_{\mathbf{i},\downarrow}^{\dagger} e^{i\mathbf{Q}_j \cdot \mathbf{r}} + \text{h.c.} \quad (\text{F1})$$

where j is summed over the three C_3 related \mathbf{Q}_i vectors. Fourier transforming to momentum space, we can compute the spectrum by defining the basis:

$$\Psi_{\mathbf{k}} = \left(c_{\mathbf{k},\uparrow}, c_{-\mathbf{k}+\mathbf{Q}_1,\downarrow}^{\dagger}, c_{-\mathbf{k}+\mathbf{Q}_2,\downarrow}^{\dagger}, c_{-\mathbf{k}+\mathbf{Q}_3,\downarrow}^{\dagger}, \dots \right) \quad (\text{F2})$$

where the ellipses denotes the continued definition of the basis, alternating between sets of spin up creation operators and sets of spin down annihilation operators such that each subsequent set of either creation or annihilation operators have an element at a momenta equal to the negative momentum plus \mathbf{Q}_j of an element in the previous set. We set a cutoff by fixing the number of these "shells", with each shell defined by a set of momenta at fixed distance from the origin when $\mathbf{k} = 0$). Within this basis, the Hamiltonian we study is constructed as

$$\mathcal{H} = \sum_{\mathbf{k}} \Psi_{\mathbf{k}}^{\dagger} \begin{pmatrix} \xi_{\mathbf{k}} & \Delta & \Delta & \Delta & \dots \\ \Delta & -\xi_{-\mathbf{k}+\mathbf{Q}_1} & 0 & 0 & \\ \Delta & 0 & -\xi_{-\mathbf{k}+\mathbf{Q}_2} & 0 & \\ \Delta & 0 & 0 & -\xi_{-\mathbf{k}+\mathbf{Q}_3} & \\ \vdots & & & & \ddots \end{pmatrix} \Psi_{\mathbf{k}} \quad (\text{F3})$$

where again the ellipses denote continued dispersion on the diagonal with alternating sign for dispersions at momenta in each shell and Δ continuing on the off diagonal coupling dispersions at momenta which sum to \mathbf{Q}_j . The absolute value of the energy of the state closest to zero energy obtained from diagonalizing Eq. F3 is shown in Fig. 9 for 17 shells of basis vectors as a function of $q = |\mathbf{Q}_i|$. The number of shells necessary to achieve convergence is on the order of k_F/q . We note the non-monotonic behavior as a function of q shown in Fig. 3 originates from the coupling between different Fermi surfaces at different q as induced by Δ .

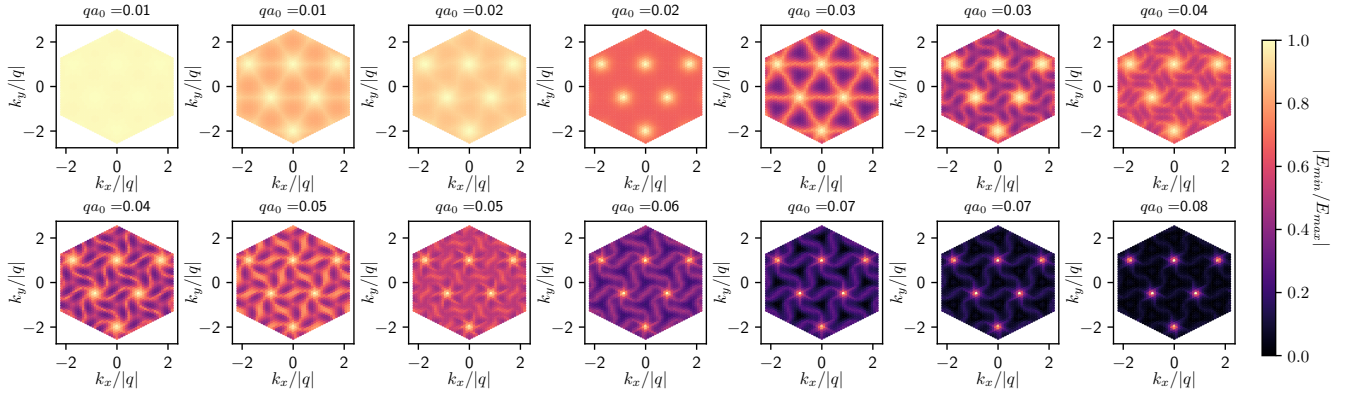


FIG. 9: We plot the energy of the lowest band of the mean-field Hamiltonian studied for the $3\text{-}\mathbf{q}$ state at $|\Delta| = .1$ meV as function of $|\mathbf{q}|$, where \mathbf{q} lies along a high symmetry contour in momentum space.